PHYSICAL REVIEW B **91**, 054419 (2015)

Simultaneous enhancements of polarization and magnetization in epitaxial $Pb(Zr_{0.52}Ti_{0.48})O_3/La_{0.7}Sr_{0.3}MnO_3$ multiferroic heterostructures enabled by ultrathin $CoFe_2O_4$ sandwich layers

Devajyoti Mukherjee,[*] Mahesh Hordagoda, Paula Lampen, Manh-Huong Phan, Hariharan Srikanth, Sarath Witanachchi, and Pritish Mukherjee

Department of Physics and Center for Integrated Functional Materials (CIFM), University of South Florida, Tampa, Florida 33620, USA

(Received 10 October 2014; revised manuscript received 4 February 2015; published 24 February 2015)

Layered thin films of $Pb(Zr_{1-x}Ti_x)O_3$ (PZT) and $La_xSr_{1-x}MnO_3$ (LSMO) are well-known multiferroic systems that show promise for numerous applications including data storage devices and spintronics. In this work, structure-property relationships are explored in novel PZT/$CoFe_2O_4$ (CFO)/LSMO heterostructures with optimized ferroic properties. High quality, epitaxial PZT/CFO/LSMO heterostructures with the thickness of the CFO layer varying from 0 to 50 nm were grown on $SrTiO_3$ (100) substrates using an optimized pulsed laser deposition technique. An ultrathin (10–20 nm) CFO layer was found to simultaneously improve the ferromagnetic and ferroelectric (FE) characteristics of the system through distinct mechanisms. The increase in magnetization and magnetic coercivity in the CFO-containing samples was associated with a tetragonal distortion of the CFO lattice under epitaxial strain, while perpendicular anisotropy generated by the distortion stabilized an out-of-plane orientation of the easy axis of magnetization in the thinnest CFO layers. Trapped charge at the CFO/PZT interface in PZT/CFO/LSMO induced an internal built-in field in the heterostructures, resulting in the accumulation of higher switched charges during voltage cycling and enhanced polarization in the samples over PZT/LSMO. An increase in electric coercivity was also observed in the CFO-containing heterostructures, and is discussed in terms of a dielectric/FE layered capacitor model. Above a critical thickness, ~50 nm, the presence of a CFO layer has a negative effect on both magnetization and polarization in PZT/CFO/LSMO as compared to PZT/LSMO.

DOI: 10.1103/PhysRevB.91.054419   PACS number(s): 77.55.Nv, 77.55.Px, 75.30.Gw, 77.55.fg

I. INTRODUCTION

Multiferroic heterostructures with coexisting and intimately coupled ferroelectric (FE) and ferromagnetic (FM) orders have attracted considerable attention in the past decade both for their technological applications in multifunctional devices and the fundamental interest in the magnetoelectric (ME) effect observed in these systems [1–10]. The mutual control of ferroelectricity and magnetism which is the long-sought goal in multiferroics is complicated by the different origins of hysteretic behaviors in FE and FM materials, often rendering the effects chemically incompatible [3]. While traditional FE materials are insulators with unfilled *d* orbitals, the existence of transition metal *d* electrons is in general necessary for magnetic ordering in FM materials. This contradiction explains the scarcity of single-phase multiferroic materials [5]. In this respect, ME composite thin films [6] comprised of layered FE and FM materials [7,8] are of special interest due to their potential applications in ME random access memories [9] and ME microsensors [10]. To date, the ME effect has been extensively reported in multiferroic layered structures in which the state-of-the-art FE perovskite $Pb(Zr_{1-x}Ti_x)O_3$ (PZT) is paired with the hard magnetic spinel-ferrite $CoFe_2O_4$ [11,12]. Typically, the observed ME coupling in piezoelectric/magnetostrictive PZT/CFO bilayered films has been attributed to their interfacial strains [13]. The presence of the CFO layer imposes an in-plane tensile stress on the PZT layer across the interface, increasing the interactive stress between the CFO and PZT layers and hence the ME coupling [6].

An alternative layered multiferroic system consists of PZT with the FM half-metallic manganite $La_xSr_{1-x}MnO_3$ (LSMO) [14,15]. The demonstration of a charge-mediated ME effect in PZT/LSMO heterostructures has revived interest in these systems for novel spintronic applications [16,17]. In addition to applications in nonvolatile data storage [18], PZT/LSMO heterostructures have recently been used to fabricate field-effect transistors [19] and FE tunnel junctions [20]. Furthermore, the use of the conducting LSMO layer as a bottom electrode during the polarization of PZT/LSMO capacitors has been shown to improve their FE and fatigue endurance properties as compared to metallic or other oxide electrodes [21]. Despite the promising properties of the PZT/LSMO system, the low magnetic coercivity of LSMO has been a deterrent for its use in certain applications including memory, where spin flipping by external stray fields could potentially destroy the stored information.

The well-known role of interfacial strain in the ME effect of PZT/CFO leads to an expectation that the incorporation of a hard ferrimagnetic CFO layer, thin enough to avoid dielectric losses ($t < 50$ nm) [22–24], in PZT/LSMO heterostructures can enhance not only the FM coercivity, but potentially the FE properties as well and consequently the ME device performance [25]. In our preliminary effort [26], interfacial strain engineering to systematically tune both the polarization and magnetization in PZT/CFO/LSMO heterostructures by varying the CFO layer thickness was not successfully demonstrated due to lack of high-quality epitaxial PZT/LSMO films with systematic control of crystallinity,

[*]Corresponding author: dmukherj@usf.edu

    ©2015 American Physical Society

stoichiometry, grain size, and surface roughness [27]. In this paper we report a simultaneous enhancement of the polarization and magnetization in PZT/CFO/LSMO as compared to PZT/LSMO heterostructures. Using our optimized pulsed laser deposition (PLD) technique, we have successfully grown epitaxial PZT/LSMO and PZT/CFO/LSMO heterostructures with ultrathin CFO sandwich layers varying from 0 to 50 nm, on $SrTiO_3$ (STO) (100) substrates. On one hand, a strain compression-relaxation mechanism has been proposed to explain the enhanced FM properties in PZT/CFO/LSMO; on the other hand, a charge-induced enhanced FE polarization was observed in PZT/CFO/LSMO as compared to PZT/LSMO heterostructures. The work provides both a fundamental understanding of the elusive structure-property relationships in these systems and the technological insight for the coherent design of future ME memory devices based on these materials.

II. EXPERIMENT

PZT/CFO/LSMO heterostructures were grown on single-crystal $SrTiO_3$ (STO) (100) substrates using a PLD technique. Briefly, high-purity ceramic targets of $La_{0.7}Sr_{0.3}MnO_3$, $CoFe_2O_4$, and $PbZr_{0.52}Ti_{0.48}O_3$ (with 40 at. % excess PbO) (Kurt J. Lesker Company) were sequentially ablated using a KrF excimer laser ($\lambda = 248$ nm, frequency = 10 Hz, fluences = 2–3 J/cm^2) inside a deposition chamber equipped with a multitarget carousel that allowed for the *in situ* deposition of multilayers with clean interfaces. A distance of 4 cm was maintained between the substrate and the targets during the depositions. In the optimized synthesis process, an initial layer of LSMO (thickness $\approx$ 100 nm) was deposited on an STO substrate at 800 °C under a background oxygen pressure (pO_2) of 10 mTorr, followed by the CFO layer (thickness $\approx$ 10, 20, 50 nm) at 450 °C with pO_2 of 10 mTorr, and the PZT layer (thickness $\approx$ 200 nm) at 550 °C under a pO_2 of 500 mTorr. Open access to the LSMO bottom electrode was maintained throughout the process using shadow masks. Finally, top LSMO electrodes of 100 μm diameter were deposited using a shadow mask at 550 °C under a pO_2 of 10 mTorr. After deposition, the PLD chamber was flooded with pure oxygen (500 mTorr) and the samples were gradually cooled down to room temperature (approximately 2 h). For comparison, PZT/LSMO heterostructures were also grown on STO substrates under the same conditions. The thicknesses of the LSMO and the PZT layers were kept constant at 100 and 200 nm, respectively.

The crystallinity and crystallographic orientations in the heterostructures were characterized by x-ray diffraction (XRD) (Bruker AXS D8 diffractometer equipped with high-resolution Lynx Eye position-sensitive detector using Cu $K\alpha$ radiation). The in-plane epitaxy was determined from XRD azimuthal (φ) scans (Philips X'pert Diffractometer). The surface morphologies were observed using an atomic force microscope (AFM) (Digital Instruments III). The interfacial microstructure in the PZT/CFO/LSMO heterostructures was analyzed using high-resolution transmission electron microscopy (HRTEM) (FEI Tecnai F 20 S-Twin TEM). The sample for cross-sectional TEM analysis was prepared by milling a 5 μm × 10 μm rectangular strip that was 100 nm in thickness from the film surface using a focused ion beam (FIB) (JOEL 4500 FIB/SEM) and Pt welding it to a Cu TEM grid. Prior to FIB milling a protective Pt layer was deposited on the film surface in order to preserve the underlying structures during cross-sectional TEM sample preparation.

Magnetic measurements were performed at room temperature using a commercial physical property measurement system (PPMS) (Quantum Design, Inc.) in magnetic fields up to 50 kOe using a vibrating sample magnetometer insert. The magnetization versus magnetic field $M(H)$ loops are reported after the subtraction of the diamagnetic contribution from the STO substrates. A home-built insert based on a precise, self-resonant tunnel-diode oscillator was integrated into the PPMS to measure transverse susceptibility of the films housed in an inductive radio-frequency (rf) coil. The shift in resonant frequency of the circuit was detected while the dc field was varied perpendicular to the rf field and parallel to the plane of the films.

The resistivity of the CFO films deposited under the same conditions on STO (100) substrates using PLD for thicknesses of 10, 20, and 50 nm were measured at room temperature in the Van der Pauw configuration using a Keithley 224 programmable current source and a Keithley 182 sensitive digital voltmeter. Room temperature polarization measurements were performed using a commercial FE tester (Precision LC, Radiant Technologies, Inc.) equipped with a microprobe station. During the hysteresis measurements, a constant standard bipolar input profile was used (100 ms hysteresis period) by varying the applied voltages from 1 to 9 V. Leakage current density versus voltage $J_L(V)$ characteristics in the thin-film capacitors were measured by applying stress voltages from 0 to $\pm$ 9 V for a soak time of 100 ms at each voltage step. Charging current density versus voltage $J_C(V)$ characteristics in the thin-film capacitors were measured using a switched-linear voltage profile starting from 0 to $\pm$ 9 V with 100 ms soak time at each voltage step, preceded by a preset pulse of $\mp$ 9 V to ensure that the linear stepping switched the polarization of the sample. Each of the preset pulses was followed by a 1 s delay time to allow any currents resulting from remanent or nonremanent polarization switching in the sample to settle and reach a steady-state value and to eliminate partial switching effects.

III. RESULTS AND DISCUSSION

A. Structure and morphology

The quality and epitaxial growth of the PZT/CFO/LSMO heterostructures grown on STO (100) and shown schematically in Fig. 1(a) were confirmed using XRD, AFM, and TEM. Heterostructures with a CFO sandwich-layer thickness of 0, 10, 20, and 50 nm are denoted hereafter as P/C(0 nm)/L, P/C(10 nm)/L, P/C(20 nm)/L, and P/C(50 nm)/L, respectively. Collectively, the series is denoted as P/C(0–50 nm)/L.

The single-crystalline nature of the P/C(0–50 nm)/L heterostructures is evidenced from their XRD θ-2θ patterns as shown in Fig. 1(b). In all cases, only (00l) (l = 1, 2, and 3) diffraction peaks of the tetragonal PZT phase (JCPDS 01-070-4060) along with the (400) peak of the face-centered cubic (fcc) CFO phase (JCPDS 00-022-1086) and the (l00) (l = 1, 2, and 3) peaks of the pseudocubic perovskite LSMO

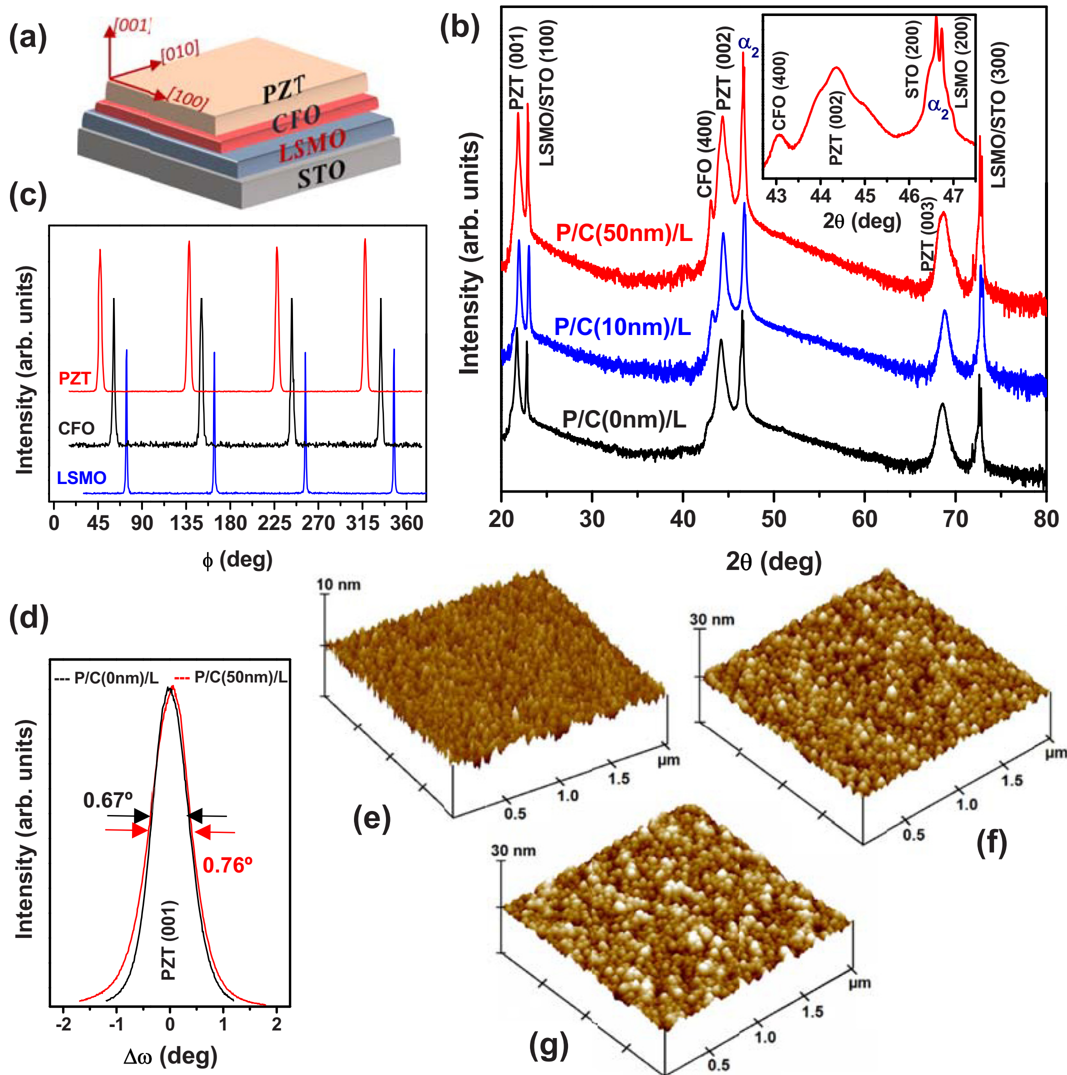

FIG. 1. (Color online) (a) Schematic of a PZT/CFO/LSMO heterostructure. (b) XRD θ-2θ patterns for heterostructures with CFO thicknesses of 0, 10, and 50 nm [P/C(0 nm)/L, P/C(10 nm)/L, and P/C(50 nm), respectively]. (c) Representative XRD azimuthal (φ) scans performed about the PZT (101), CFO (311), and LSMO (110) crystallographic planes. (d) Rocking curves performed about the PZT (001) crystallographic plane for P/C(0 nm)/L and P/C(50 nm)/L. AFM images of (e) LSMO in P/C(50 nm)/L, (f) PZT in P/C(0 nm)/L, and (g) PZT in P/C(50 nm)/L.

phase (JCPDS 01-089-4461) are observed, indicating the epitaxial growth of the individual layers [26,28]. No secondary phase formations are present within the resolution limits of the instrument. Azimuthal (φ) scans were performed about the PZT (101), CFO (311), and LSMO (110) crystallographic planes to confirm the in-plane epitaxial relationships of the P/C(0–50 nm)/L heterostructures. Figure 1(c) shows a representative φ pattern; the occurrence of peaks at regular intervals of 90° is a consequence of the fourfold cubic symmetry of the individual layers in the heterostructures. Rocking curves performed about the PZT (001) crystallographic planes for P/C(0 nm)/L and P/C(50 nm)/L [Fig. 1(d)] yield peaks with a narrow FWHM ($0.67^\circ \leqslant \Delta\omega \leqslant 0.76^\circ$), confirming the excellent in-plane orientation of the PZT layers. It can be seen that the introduction of a CFO layer does not reduce the degree of in-plane orientation of the PZT layers.

The LSMO bottom layers in P/C(0–50 nm)/L show an extremely smooth morphology with root-mean-square roughness (R_{rms}) as low as 1–2 nm and uniform grain sizes ($\approx 60 \pm 9$ nm). A representative AFM image [Fig. 1(e)] is shown on the exposed surface of the LSMO bottom layer in P/C(50 nm)/L [29]. The excellent quality of the LSMO surface provides an optimal platform for the growth of the overlaying CFO and PZT layers. The smooth and particulate-free surfaces of the topmost PZT layers are shown in Figs. 1(f) and 1(g) for P/C(0 nm)/L and P/C(50 nm)/L, respectively. While the surface roughness ($R_{\mathrm{rms}} \approx$ 4–6 nm) and uniform grain size $\approx 170 \pm 10$ nm for P/C(0 nm)/L matches well with earlier reports [30], only a slight increase in the surface roughness ($R_{\mathrm{rms}} \approx$ 6–8 nm) is found for P/C(50 nm)/L. The distinct grain growth on the PZT surfaces suggests a relaxation of the epitaxial strain in the 200 nm PZT layers.

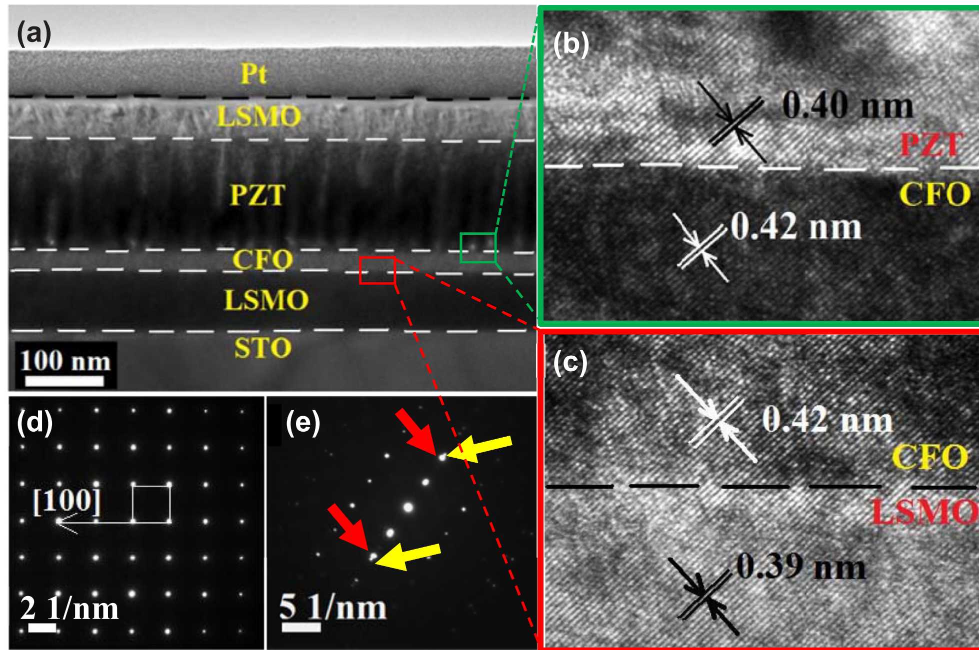

FIG. 2. (Color online) (a) Cross-sectional TEM image of P/C(20 nm)/L. (b) and (c) HRTEM images of the PZT-CFO and the CFO-LSMO interfaces in the regions marked by green and red boxes in (a). (d) and (e) SAED patterns near the CFO-LSMO and the PZT-CFO interfaces of P/C(20 nm)/L heterostructure. The cubic unit cell is marked by a white box with an arrow pointing along the *a* axis.

The single-crystalline nature and the cube-on-cube epitaxial growth morphology of the individual layers in P/C(0–50 nm)/L are further confirmed via electron microscopy. A representative cross-sectional TEM image of P/C(20 nm)/L in Fig. 2 (a) reveals sharp and flat interfaces between PZT-CFO, CFO-LSMO, and LSMO-STO. The thicknesses of the individual layers of the heterostructure, as well as those of the LSMO top-electrode layer and the Pt capping layer, are uniform. Figures 2(b) and 2(c) show HRTEM images of the PZT-CFO and the CFO-LSMO interfaces in the regions enclosed by green and red boxes in Fig. 2(a), respectively. The high-resolution images demonstrate atomically sharp and flat phase boundaries with continuous lattice fringes from the intermediate CFO layer to the top PZT layer [Fig. 2(b)], and from the bottom LSMO layer to the intermediate CFO layer [Fig. 2(c)]. Similar HRTEM images at different locations along these interfaces and along the LSMO-STO interface (see our earlier report [31]) showed no evidence of any structural defects such as lattice misfits or twin planes. The *d* spacings determined from HRTEM are consistent with those obtained from XRD. The selected area electron diffraction (SAED) patterns acquired near the CFO-LSMO and the PZT-CFO interfaces shown in Figs. 2(d) and 2(e), respectively, confirm the single-crystalline nature of the layers and their cubic symmetry. The SAED pattern near the PZT-CFO interface shows slightly displaced lattice planes [marked by red and yellow arrows in Fig. 2(e)] indicating a lattice mismatch between the PZT and the CFO layers, also evident from the XRD analysis.

B. Strain analysis

In-plane ($a_{||}$) and out-of-plane ($a_{\perp}$) lattice parameters were calculated for the individual layers in the P/C(0–50 nm)/L heterostructures using XRD asymmetric (2θ-ω) scans and symmetric (θ-2θ) scans performed about multiple crystallographic planes in LSMO, CFO, and PZT. The lattice parameters of the LSMO layers ($a_{||} = 3.897$ Å and $a_{\perp} = 3.887$ Å) are very close to those of the STO substrates ($a_{\perp} = a_{||} = 3.905$ Å), consistent with their epitaxial growth observed above [27,29,32]. The lattice parameters of the PZT layers ($a_{||} = 4.055$ Å and $a_{\perp} = 4.11$ Å) are similar to the parameters of the bulk material, confirming the strain relaxation suggested by Figs. 1(f) and 1(g). This finding is in good agreement with an earlier report that found a critical thickness of 80 nm for complete strain relaxation in epitaxial PZT layers [33].

The thickness of the CFO sandwich layer strongly affects its lattice parameters and the distortion of the unit cell. In Figs. 3(c) and 3(f), asymmetric scans of P/C(10 nm)/L show a significant shift of the CFO (311) and (511) peaks to higher 2θ values with respect to the bulk peak positions. This can be attributed to an in-plane compression of $a_{||}$ in the CFO layer to match the smaller lattice parameter of the underlying LSMO layer during epitaxial growth. The compressive strain relaxes as the thickness of the CFO layer increases, and the (311) and (511) peaks shift closer to their bulk positions in P/C(20 nm)/L [Figs. 3(b) and 3(e)] and P/C(50 nm)/L [Figs. 3(a) and 3(d)]. In order to accommodate reduced $a_{||}$, the CFO unit cell in P/C(10–50 nm)/L undergoes a volume-conserving out-of-plane expansion (i.e., an increase in $a_{\perp}$), manifested as a peak shift to lower 2θ values in symmetric scans about the CFO (400) plane in Figs. 4(a)–4(c). Increasing the thickness of the CFO layer from 10 to 50 nm relieves the tetragonal distortion of the CFO unit cell, and $a_{\perp}$ approaches the bulk lattice parameter as illustrated in Fig. 4(d).

The calculated $a_{\perp}$ and $a_{||}$ values and the tetragonal distortion ($a_{\perp}/a_{||} - 1$) of the CFO unit cell in P/C(10–50 nm)/L

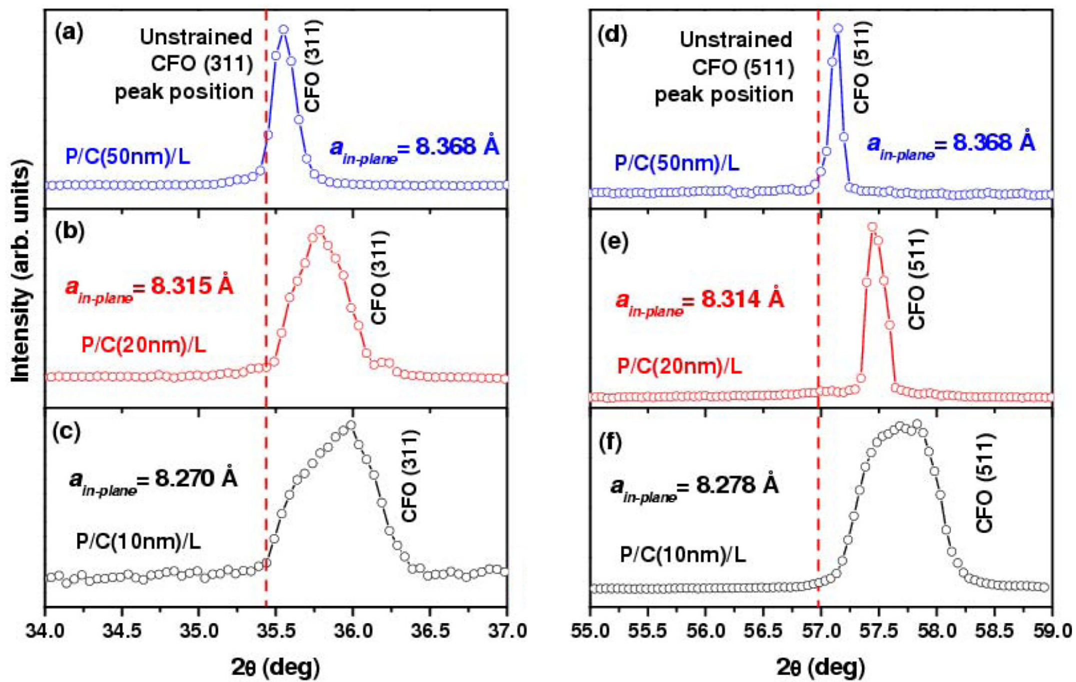

FIG. 3. (Color online) Asymmetric 2θ-ω XRD scans performed about the CFO (311) (left panel) and CFO (511) (right panel) crystallographic planes for (a) and (d) P/C(50 nm)/L, (b) and (e) P/C(20 nm)/L, and (c) and (f) P/C(10 nm)/L heterostructures. CFO (311) and (511) planes were chosen to avoid contributions from underlying LSMO or overlying PZT layers. Unstrained bulk CFO peak positions are indicated by dashed lines.

are summarized in Table I. Based on the lattice parameters, out-of-plane ($\varepsilon_\perp$) and in-plane ($\varepsilon_{||}$) strains in the CFO layer were calculated according to $\varepsilon = (a - a_o)/a_o$, where a is $a_\perp$ or $a_{||}$ and $a_o = 8.391$ Å is the bulk unstressed lattice parameter of CFO determined from the powder XRD pattern. The in-plane stress $\sigma_{||} = Y\varepsilon_{||}$ (where Y = Young's modulus of CFO, $Y_{100} = 1.5 \times 10^{12}$ dyn/cm^2) [34] and the magnetoelastic stress anisotropy $K_a = (3/2)\lambda_{100}\sigma$ (where $\lambda_{100} =$

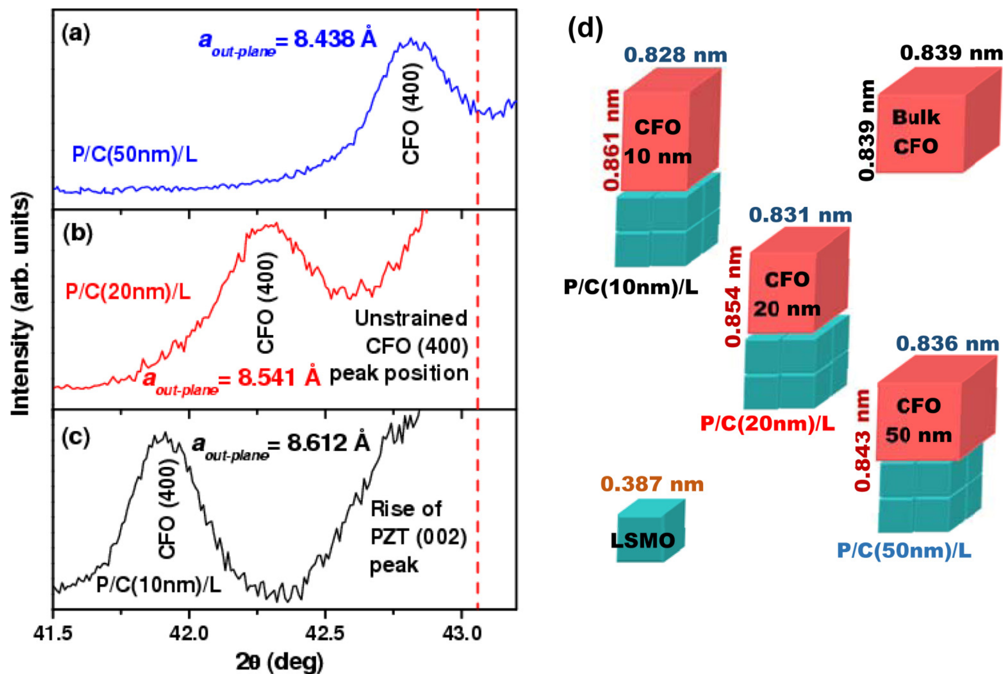

FIG. 4. (Color online) Symmetric θ-2θ XRD scans performed about the CFO (400) crystallographic plane for (a) P/C(50 nm)/L, (b) P/C(20 nm)/L, and (c) P/C(10 nm)/L heterostructures. The unstrained bulk CFO (400) peak position is indicated by a dashed line. (d) Schematic diagram illustrating the tetragonal distortion of the fcc CFO bulk lattice ($a = 0.839$ nm) in the heterostructures. The in-plane and out-of plane lattice parameters were calculated from the asymmetric and symmetric XRD scans, respectively.

TABLE I. Structural and strain parameters in P/C(10–50 nm)/L heterostructures determined from XRD as detailed in the text: out-of-plane ($\perp$) and in-plane ($||$) lattice parameters (a), tetragonal distortion, strain (ε), stress ($\sigma_{||}$), and magnetoelastic stress anisotropy (K_a).

Sample	Lattice parameters $a_\perp$ (Å)	$a_{||}$ (Å)	Distortion $(a_\perp - a_{||})/a_{||}$ (%)	Strain $\varepsilon_\perp$	$\varepsilon_{||}$	Stress $\sigma_{||} = Y_{\varepsilon_{||}}$ ($\times 10^{10}$ dyn/cm^3)	Anisotropy K_a ($\times 10^7$ erg/cm^3)
P/C(10 nm)/L	8.612	8.280	4.01	0.026	−0.013	−1.95	−1.73
P/C(20 nm)/L	8.541	8.315	2.72	0.018	−0.009	−1.35	−1.19
P/C(50 nm)/L	8.438	8.368	0.83	0.006	−0.003	−0.45	−0.39

-590×10^{-6} is the magnetostriction coefficient for CFO [35]) are also given in Table I. It is clear that P/C(10 nm)/L exhibits the highest tetragonal distortion due to in-plane compressive and out-of-plane tensile strains which result in its higher magnetoelastic stress anisotropy as compared to P/C(20 nm)/L and P/C(50 nm)/L. The tetragonal distortion of the CFO layer influences the magnetic performance of the heterostructures as discussed below.

C. Strain-mediated magnetization enhancement and anisotropy reorientation

In Fig. 5, a clear enhancement of magnetization in the heterostructures with an ultrathin (10–20 nm) CFO layer over the PZT/LSMO heterostructure is demonstrated in the room temperature in-plane $M(H)$ loops for P/C(0–50 nm)/L (see Table II). While the saturation magnetization $M_S = 395\,\text{emu/cm}^3$ and coercivity $H_C = 0.1\,\text{kOe}$ for P/C (0 nm)/L are in good agreement with previously reported values for epitaxial PZT/LSMO thin films [15,27], an increase in both

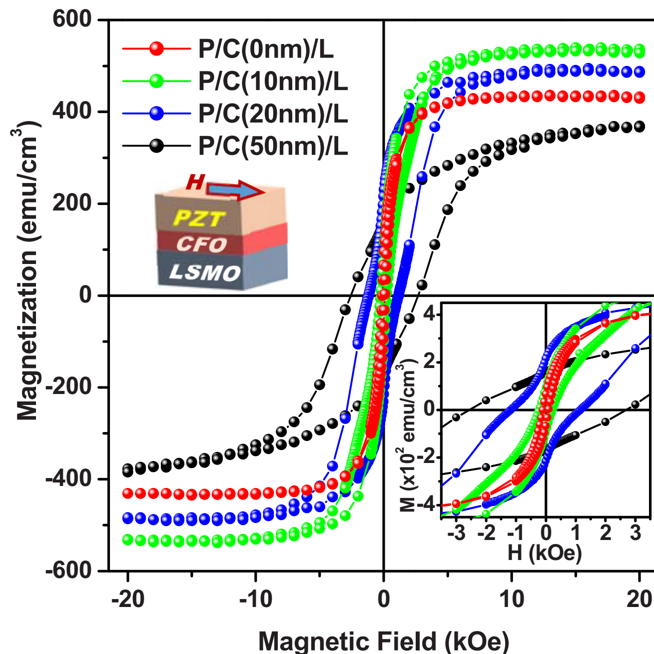

FIG. 5. (Color online) In-plane magnetic hysteresis $M(H)$ loops at 300 K for P/C(0–50 nm)/L heterostructures. Insets show the schematic diagram of the PZT/CFO/LSMO heterostructure and the enlarged low-field $M(H)$ curves.

ferromagnetic figures of merit results when a 10 nm ($M_S = 536\,\text{emu/cm}^3$, $H_C = 0.3\,\text{kOe}$) or 20 nm ($M_S = 488\,\text{emu/cm}^3$, $H_C = 1.2\,\text{kOe}$) intermediate CFO layer is introduced in the system. It is interesting to note that the greatest increase in the magnetization of the heterostructure is associated with the thinnest CFO layer (10 nm). When the thickness of the CFO layer is doubled to 20 nm, the magnetization of the heterostructure decreases somewhat while the coercivity continues to increase by a factor of ~4. Between 20 and 50 nm, the magnetization of PZT/CFO/LSMO drops below that of the PZT/LSMO system. The characteristics of P/C(50 nm)/L ($M_S = 380\,\text{emu/cm}^3$, $H_C = 3.0\,\text{kOe}$) are comparable to those of epitaxial PZT/CFO thin films with a 100 nm CFO layer grown on STO (100) substrates ($M_S = 360\,\text{emu/cm}^3$, $H_C = 3.1\,\text{kOe}$ [28]), indicating that above 50 nm the CFO layer dominates the magnetic properties of the heterostructures. From a device standpoint the ferromagnetic properties of the heterostructures can be considered optimized by a 20 nm CFO layer, for which a 12-fold increase in H_C in the PZT/CFO/LSMO system over the PZT/LSMO system is combined with an enhancement in M_S exceeding 20%.

The tuning of the magnetic properties of the P/C(0–50 nm)/L series with CFO layer thickness can be attributed to the combined influences of changing magnetic volume (accounted for in the normalization of magnetization), interfacial magnetic coupling, and stress. The effect of stress (σ) on the magnetization of a magnetostrictive material such as CFO can be understood from the following thermodynamic relation [36]:

$$\frac{1}{l}\frac{\partial l}{\partial H} = \frac{\mu_o}{4\pi}\frac{\partial M}{\partial \sigma} \tag{1}$$

where M is the magnetization, μ_o is the permeability of free space, σ is the stress, $\partial l/l$ is the magnetostriction of the material, and H is the external applied magnetic field. From Eq. (1), the magnetization in CFO, a negative magnetostrictive material (i.e., $\Delta l/l < 0$), will be increased by compressive stress (i.e., $\partial\sigma < 0$), as reported earlier in epitaxial CFO thin films [37]. The trend of decreasing in-plane magnetization with increasing CFO layer thickness for the P/C(10–50 nm)/L series mirrors that of the in-plane compressive stress, which relaxed as the CFO thickness increased (Table I), establishing a clear correlation between the stress and magnetization in these heterostructures. The strong development of coercivity with CFO layer thickness is expected based on the increase in total hard magnetic volume in the heterostructures.

To characterize magnetic anisotropy in the PZT/CFO/LSMO heterostructures, a comparison of room temperature

TABLE II. Ferromagnetic and ferroelectric characteristics of P/C(0–50 nm)/L heterostructures: saturation magnetization (M_S), squareness (M_r/M_S)) (where M_r is remanent magnetization), magnetic coercivity (H_C), saturation polarization (P_S), remanent polarization (P_r), switching voltages ($\pm V_c$), and electric coercivity (E_C).

	Ferromagnetic properties				Ferroelectric properties			
Sample	M_{sat} (emu/cm^3)	M_r/M_{sat} (%)	H_c (kOe)	P_{sat} (μC/cm^2)	P_r (μC/cm^2)	V_c (+) (V)	V_c (−) (V)	E_c (kV/cm)
P/C(0 nm)/L	432 ± 3	15.4	0.1	60	52	1.86	1.84	92.5
P/C(10 nm)/L	536 ± 2	17.1	0.3	90	78	2.93	1.89	114.8
P/C(20 nm)/L	488 ± 4	47.3	1.2	85	68	3.19	1.98	117.5
P/C(50 nm)/L	380 ± 2	41.6	3.0	45	40	5.31	3.82	182.6

$M(H)$ loops for in- and out-of-plane orientations of the applied magnetic field is made in Fig. 6. P/C(0 nm)/L exhibits an easy-plane behavior, with a slow approach to saturation for a field applied out-of-plane, marking the c axis as a hard magnetization direction. With the introduction of an ultrathin CFO sandwich layer, an easy direction is no longer well defined for the heterostructure [Figs. 6(b) and 6(c)]. A saturated value of magnetization is reached at similar applied fields in the in-plane and out-of plane directions, although the out-of-plane M_S is smaller than the in-plane M_S. This observation can be related to the strong tetragonal distortions of the ultrathin CFO layers, which generate a perpendicular magnetocrystalline anisotropy. An out-of-plane easy axis of magnetization is stabilized by perpendicular anisotropy sufficient to overcome the shape anisotropy, which favors an easy plane. A thickness dependent reorientation of magnetic anisotropy has been observed previously in epitaxial CFO thin films [38,39]. Our observations are consistent with such a scenario, illustrated schematically in the insets of Fig. 6. In the highly distorted P/C(10 nm)/L, an out-of-plane easy axis in the CFO layer would produce the ready saturation of out-of-plane magnetization seen in Fig. 6(b). On the other hand, the lattice relaxation towards the cubic structure of bulk CFO in P/C(50 nm)/L allows the shape anisotropy to dictate that the easy direction of the CFO layer lies in the ab plane, once again establishing a well-defined anisotropy direction for the heterostructure as observed in Fig. 6(d). The validity of this scenario relies on the unchanging in-plane magnetic anisotropy of the underlying LSMO layers.

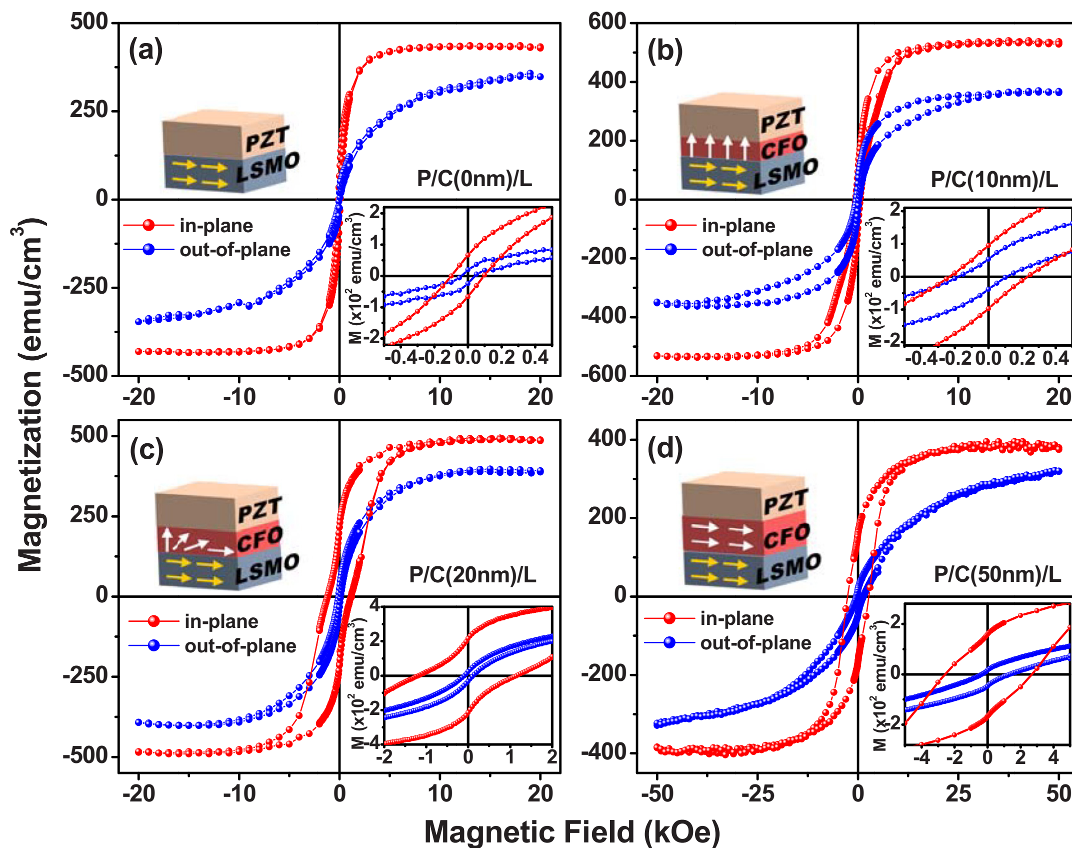

FIG. 6. (Color online) In-plane and out-of-plane magnetic hysteresis loops at 300 K for (a) P/C(0 nm)/L, (b) P/C(10 nm)/L, (c) P/C(20 nm)/L, and (d) P/C(50 nm)/L. Insets show enlarged low-field $M(H)$ curves and the relative orientation of the magnetic anisotropies in the CFO and LSMO layers as discussed in the text.

To confirm the reorientation of the easy axis in the ultrathin CFO layers, we have employed a radio-frequency transverse susceptibility χ_T technique, which has recently been utilized to directly measure the effective anisotropy and switching fields in a variety of systems including thin films, nanoparticles, and single crystals [40–42]. The sample is housed in an inductive rf coil, which generates a small amplitude (<5 Oe) ac field H_{ac} to perturb the magnetization of the sample. The change in the resonant frequency of the circuit under the influence of a changing external dc magnetic field H can be directly related to the sample susceptibility through the inductance. The relative change in transverse susceptibility is expressed by

$$\frac{\Delta\chi_T}{\chi_T}(\%) = \frac{\chi_T(H_{\max}) - \chi_T(H)}{\chi_T(H_{\max})} \times 100, \qquad (2)$$

where $H_{\max}$ is the maximum applied dc magnetic field. A $\chi_T(H)$ curve for a conventional ferromagnetic material in which H (where is H is perpendicular to the easy axis) is swept from positive to negative saturation shows singularities at the anisotropy fields ($H = \pm H_k$) and the switching field ($H = H_s$) [43]. We note that in practice the switching peak or anisotropy peaks may be absent from the χ_T profile, depending on the magnetic nature of the sample [37,44–47].

The $\chi_T(H)$ curves of P/C(10 nm)/L and P/C(50 nm)/L were measured with H applied in the plane of the film. This configuration ($H_{ac} \| c$) allows the effective anisotropy and switching behavior to be probed in the out-of-plane (transverse) direction. Figure 7(a) shows representative χ_T data recorded as the dc field was swept from positive (+20 kOe) to negative (–20 kOe) saturation. A sharp peak in the susceptibility near zero magnetic field in P/C(10 nm)/L, due to presence of magnetically soft LSMO, is accompanied by shoulders at ∼±5 kOe. The symmetric nature of the features and their location indicate that they are related to the anisotropy fields ($\pm H_k$) of the CFO layer. The appearance of these anisotropy peaks is a direct confirmation of the out-of-plane orientation of the easy axis in the 10 nm CFO layer. High resolution bipolar χ_T data for P/C(10 nm)/L are shown in Fig. 7(b), revealing a single peak at $H\sim 0$ in each field-direction sweep. The absence of a second set of out-of-plane anisotropy peaks associated with LSMO confirms the perpendicular orientations of the LSMO and CFO layer anisotropies for P/C(10 nm)/L proposed above. In Fig. 7(a), shoulders are not observed in the $\chi_T(H)$ curve of P/C(50 nm)/L, consistent with the expectation that the easy axis of the 50 nm CFO layer lies in-plane and is therefore not perturbed by the rf field in the current measurement geometry.

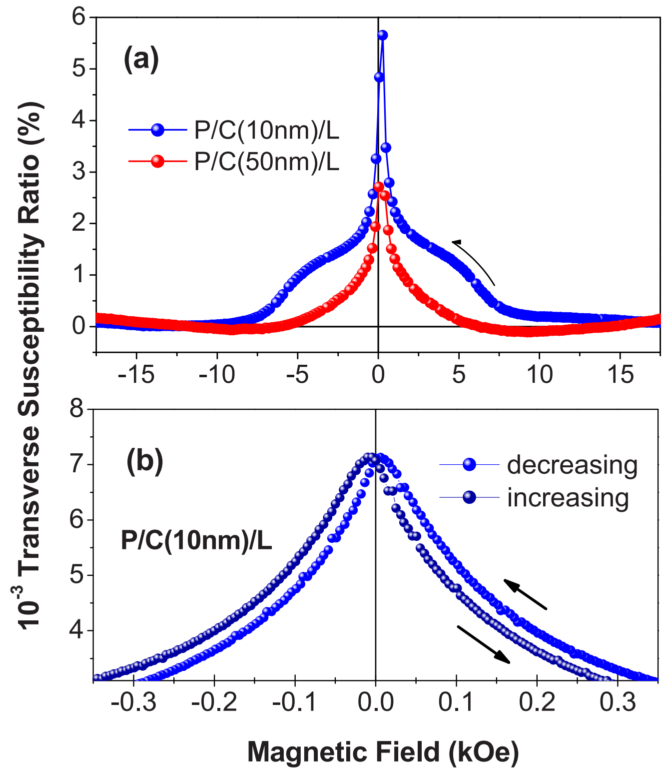

FIG. 7. (Color online) (a) Unipolar (+20 kOe → −20 kOe) transverse susceptibility ratio vs magnetic field curves for P/C(10 nm)/L and P/C(50 nm)/L, with the magnetic field applied in-plane. (b) High resolution bipolar scan of the low-field region of P/C(10 nm)/L.

D. Internal-field-mediated enhancement of ferroelectric properties

To determine the effect of the CFO layer and its thickness on the ferroelectric properties of P/C(0–50 nm)/L, FE capacitors were fabricated from the heterostructures by depositing several LSMO top electrodes (100 μm pads), and using an exposed portion of the conducting LSMO layer as the bottom electrode. Figure 8 shows polarization hysteresis loops with maximum applied voltage varying from 1 to 9 V for the P/C(0–50 nm)/L capacitors. Well-saturated, square hysteresis was observed for all devices above a nominal applied voltage which increased with CFO layer thickness from 3 V for P/C(0 nm)/L to 6 V for P/C(50 nm)/L, clearly indicating the increasing switching fields required to pole the devices. The well-behaved FE polarization is attributed to the single-crystalline nature of the heterostructures and the defect-free nature of their interfaces. Both saturation polarization P_S and remanent polarization P_r increase in the P/C(0 nm)/L device with increasing applied voltages while the coercive field E_C remains approximately constant. Increasing variation in P_r and E_C is observed in P/C(10–50 nm)/L due to pronounced space-charge effects in these heterostructures [48].

The $P(V)$ curves measured between ± 9 V are plotted in Fig. 9(a). The ferroelectric characteristics of P/C(0 nm)/L ($P_r = 52\,\mu\mathrm{C/cm^2}$ and $E_C = 30\,\mathrm{kV/cm}$) are consistent with earlier reports for epitaxial PZT films of the same composition [49,50]. Compared to the PZT/LSMO system, enhanced polarization is found in the heterostructures with an ultrathin (10–20 nm) CFO sandwich layer. Analogous to the trend in the magnetization, the highest remanent polarization ($P_r = 78\,\mu\mathrm{C/cm^2}$) is generated by the addition of a 10 nm CFO layer. P_r decreases somewhat for a 20 nm CFO layer ($P_r = 68\,\mu\mathrm{C/cm^2}$), and drops below the rest of the series in the 50 nm layer (Table II). The $P(V)$ curves for P/C(10–50 nm)/L show the presence of a built-in field ($V_{c(+)} > -V_{c(-)}$), in contrast to the symmetric curve for P/C (0 nm) /L ($V_{c(+)} \approx -V_{c(-)}$). This field is associated with the insulating character of the

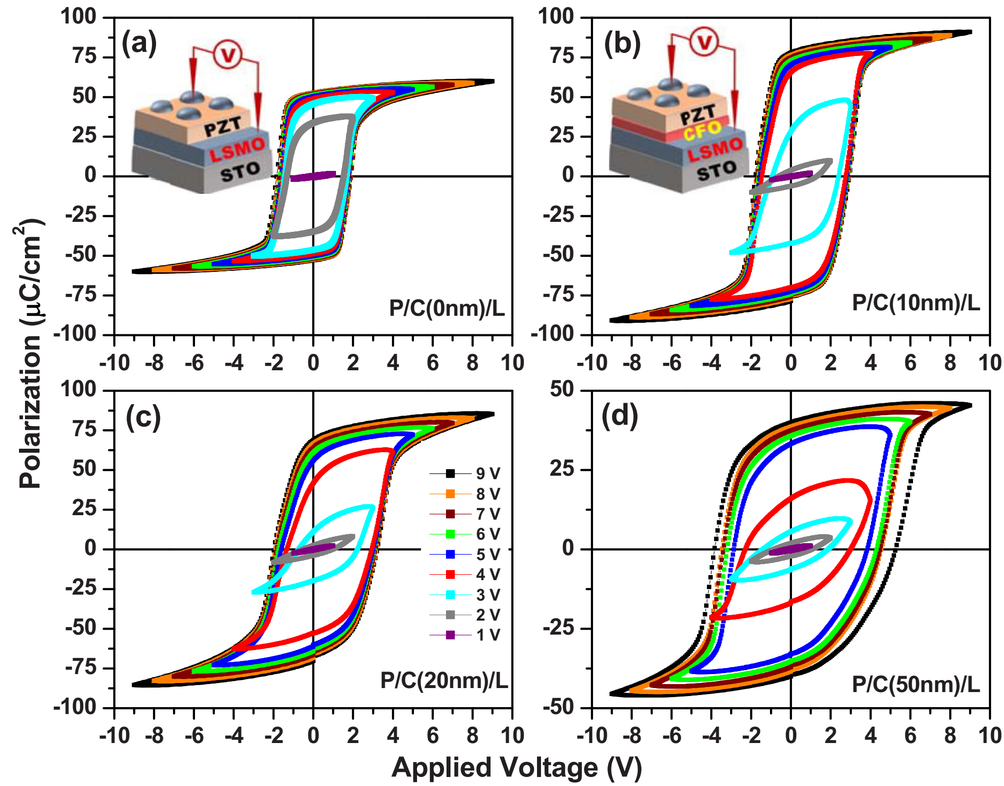

FIG. 8. (Color online) Polarization vs applied voltage $P(V)$ loops for (a) P/C(0 nm)/L, (b) P/C(10 nm)/L, (c) P/C(20 nm)/L, and (d) P/C(50 nm)/L, measured at applied voltages varying from 1 to 9 V at 1 kHz. The capacitors geometry is illustrated in the insets to (a) and (c).

intermediate CFO layer separating the bottom LSMO electrode and the PZT layer. The resistivity of CFO in P/C(10 nm)/L was high ($\rho = 2.03 \times 10^9\ \Omega$ cm), and decreased as the CFO layer thickness increased from 10 to 20 nm ($\rho = 4.53 \times 10^8\ \Omega$ cm) and 50 nm, consistent with earlier reports [51].

The ferroelectric characteristics of the PZT/CFO/LSMO series can be modeled by considering a layered capacitor structure [Fig. 9(b), inset] with a FE layer (PZT) of thickness L (200 nm) and a nonswitching insulating layer (CFO) of thickness d (with $d < L$). The electric field E required for polarization switching is given by [52]

$$E = E_f + (d/L)E_d, \quad (3)$$

where E_f and E_d are the electric fields seen by the FE and dielectric layers, respectively. From Eq. (3), the direct dependence of E on d accounts for the increase in polarization switching field with CFO thickness observed in Fig. 8. Assuming that E_d is sufficient to provoke charge injection from the adjacent LSMO electrode during voltage cycling (i.e., $E_d > E_{\text{th}}$, where E_{th} is the threshold field of charge injection) [53], the coercive field of the layered capacitor device is greater than the coercive field due to the FE layer (E_{C0}), E_C is related to E_{C0} by [54]

$$E_C = E_{C0} + (d/L)\, E_{\text{th}}. \quad (4)$$

Equation (4) accounts for the increasing trend in experimental E_C values (Table II), calculated as $E_C = (V_{c(+)} + V_{c(-)})/(d + L)$, for the P/C(0–50 nm)/L heterostructures with increasing CFO layer thickness, and validates the appearance of charge injection at the CFO/LSMO interface. Injected charge trapped at the boundary between the dielectric CFO and the FE PZT layers generates the built-in fields observed in Fig. 9(a). The trapped-charge-induced built-in field at a dielectric/FE interface can affect the FE switching behavior in these heterostructures [55].

Leakage current in PZT FE thin film capacitors is influenced by injected charge entrapment [56], as evidenced from the leakage current density versus voltage $J_L(V)$ characteristics for the P/C(0–50 nm)/L capacitors shown in Fig. 9(b). While the leakage currents for P/C(0 nm)/L are in good agreement with those of standard PZT thin films [57], higher leakage currents with increasing thickness CFO layer thickness can be attributed to the reduced resistivity of the CFO layer as its thickness increases from 10 to 50 nm [22]. The asymmetric nature of the branches in the leakage curves for P/C(10–50 nm)/L reflects the dissimilar intrinsic properties (e.g., interface state densities and potential barrier heights) of the two electrode-film interfaces in the capacitors, which affect the interface-controlled injection of carriers [58].

The FE switching behavior in the P/C(0–50 nm)/L capacitors is observed in Fig. 9(c) in the charging current density versus voltage $J_C(V)$ characteristics measured using low frequency switched-linear ac voltage cycling. Neglecting any transient current contribution due to the aging effect J_A, which normally appears under high fields and/or at high temperatures, the charging current density J_C is given by [59]

$$J_C = J_S + J_L (J_A \ll J_L < J_S), \quad (5)$$

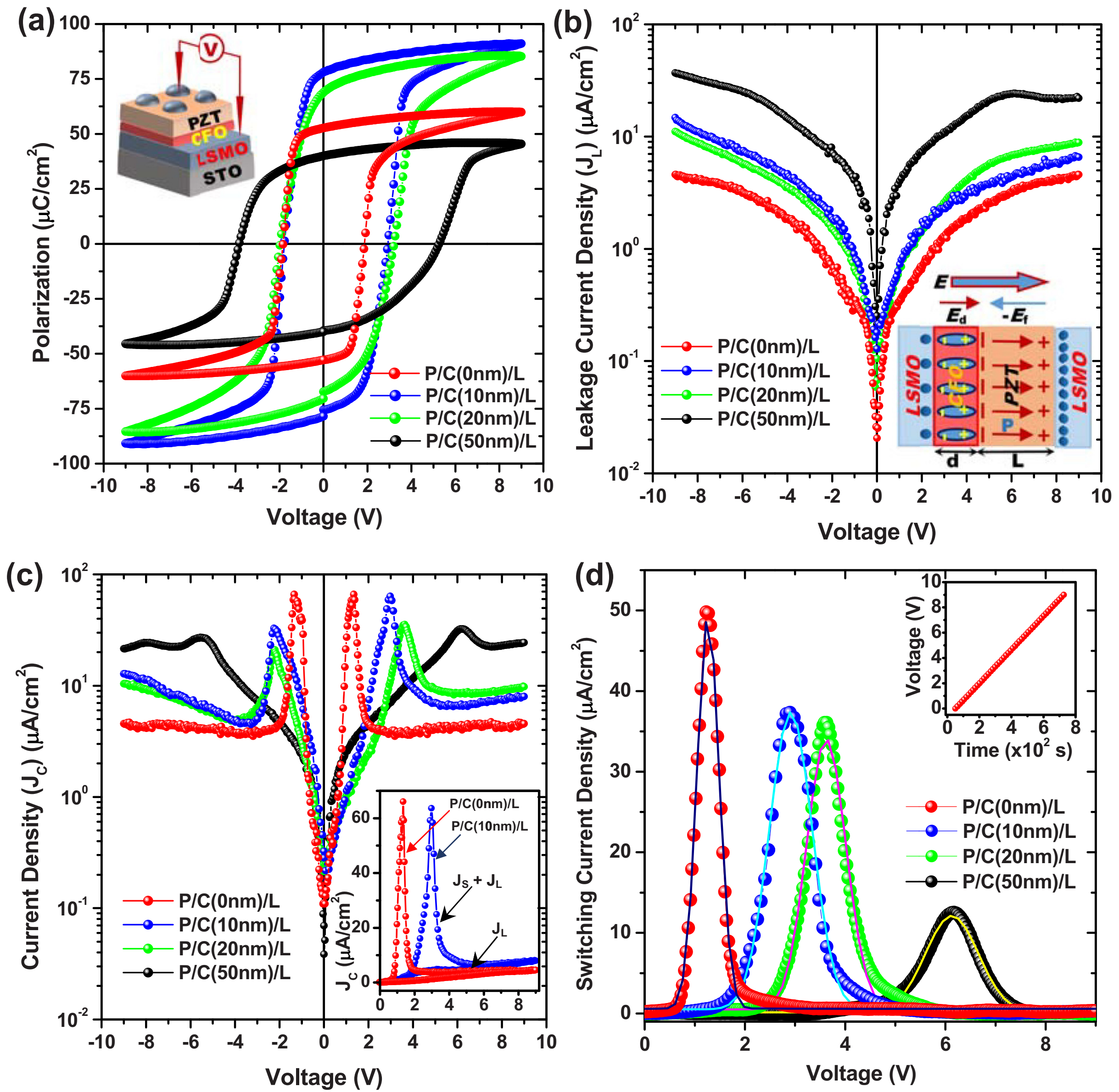

FIG. 9. (Color online) (a) Polarization hysteresis loops at 300 K for P/C(0–50 nm)/L recorded at 1 kHz using an applied voltage of 9 V. (b) Leakage current vs voltage $J_L(V)$. Inset: Model sandwich capacitor used for the description of FE switching behavior. (c) Charging current vs voltage $J_C(V)$. Inset: Charging current and leakage densities in the positive voltage cycling for P/C(0 nm)/L and P/C(10 nm)/L heterostructures. (d) FE switching current densities vs voltage $J_S(V)$, with a Gaussian fit (solid lines). Inset: Voltage profile used during $J_C(V)$ measurements.

where J_S is the transient current associated with the polarization switching. The peaks in the $J_C(V)$ curves are associated with the switching currents and occur at the nominal switching voltages $\pm V_c$. Since the reversed-voltage pulse (± 9 V) applied prior to each J_C measurement in order to switch the polarization state in the capacitors was much higher than their E_C, the current peaks in the $J_C(V)$ curves in Fig. 9(c) represent fully switched states. The asymmetry with respect to peak positions/heights in the characteristic curves of P/C(10–50 nm)/L can be attributed to the built-in fields associated with a CFO layer. The inset to Fig. 9(c) shows the overlapped $J_C(V)$ and $J_L(V)$ curves in the positive voltage cycle for P/C(0 nm)/L and P/C(10 nm)/L. The true switching currents can be extracted by subtracting the background J_L contributions from the J_C curves.

In terms of ferroelectric device performance, the important consequence of an added ultrathin CFO layer in PZT/LSMO heterostructures is the built-in electric field developed due to charge injection and entrapment across the PZT/CFO interface. The built-in field assists the FE switching, resulting in higher switched charge and, consequently, the enhanced polarization observed in the P/C(10 nm)/L and P/C(20 nm)/L heterostructures. The internal field and switched charge for the P/C(0–50 nm)/L capacitors can be quantified by examining the switching current density versus voltage $J_S(V)$ characteristics in Fig. 9(d). A broadening of the $J_S(V)$ curves with

TABLE III. Integrated area and Gaussian fitted parameters of switching current data in the positive voltage cycle for P/C(0–50 nm)/L heterostructures.

	Gaussian Fitting Parameters				
Sample	Area ($\equiv Q\ S$) ($\times 10^{-5}$)	Center ($\approx V c$) (V)	Width ($\approx \Delta\ V$) (V)	Height (J_S max) ($\times 10^{-5}$)	Integral ($\equiv$ switched charge) ($\times 10^{-5}$)
P/C(0 nm)/L	2.69	1.26	0.44	4.89	3.23
P/C(10 nm)/L	3.96	2.91	0.86	3.69	4.43
P/C(20 nm)/L	3.32	3.62	0.79	3.36	3.78
P/C(50 nm)/L	1.59	6.13	1.06	1.19	1.72

decreasing peak heights (J_S max values) occurs with increasing CFO layer thickness. According to the Preisach model for FE thin film capacitors [60], such a broadening of switching current peaks during voltage cycling is primarily associated with a spatially nonuniform internal bias field present in a capacitor as a result of charge entrapment. The other factors which can influence the switching currents—random fields due to structural defects in the films and nonuniform fields due to thickness variations or spatially random orientation of polar axes in polycrystalline samples—can be considered insignificant in the epitaxial P/C(0–50 nm)/L heterostructures [61]. The $J_S(V)$ curves were fitted with a Gaussian distribution [62] to estimate the internal built-in field (width of distribution), nominal switching voltage (center of distribution), and maximum switching current $J_{S\max}$ (height of the distribution) in the P/C(0–50 nm)/L heterostructures. The built-in and coercive fields are found to increase consistently while $J_{S\max}$ decreases as the CFO thickness increases (Table III). The switched charge is estimated by integrating the $J_S(V)$ curves according to

$$Q_S = \int_0^t J_S\,[V(t)]\,dt, \tag{6}$$

where t is time, since the voltage profile $V(t)$ linearly varies with time as shown in the inset of Fig. 6(d). The Gaussian fitted parameters and calculated switched charges for P/C(0–50 nm)/L are listed in Table III. The switched charges for P/C(10 nm)/L and P/C(20 nm)/L are larger than in P/C(0 nm)/L, while the switched charge in P/C(50 nm)/L is less than in P/C(0 nm)/L. This observation explains the trend in polarization for the series, since the FE hysteresis loop represents the integral of the charge released during the polarization switching [63].

To date, there have been several observations of strong ME effect in PZT/LSMO layered thin films. The highest values of ME voltage coefficient α_E in epitaxial PZT/LSMO bilayers (60–70 mV/cm Oe) are much larger than those of any single-phase ME material on record [14,16,64,65]. In contrast to multiferroic composite systems that depend on strain to couple the FM and FE orders, the ME coupling in PZT/LSMO layered thin films is charge mediated and electronic in origin [14,16]. The sensitivity of the strongly correlated electronic and spin states of the manganite phase to charges in the carrier doping of the LSMO layer provides enhanced coupling between the FM and FE order parameters. The large transverse ME coefficient in PZT/LSMO (-13.5 Oe cm kV^{-1} at 180 K) arises from changes in the magnetization of the LSMO layer as the PZT polarization is switched, driving the system into the accumulation or depletion state [66]. Given the established charge-mediated ME coupling in PZT/LSMO, the insertion of the ultrathin CFO layer might be expected to enhance the ME effect in PZT/CFO/LSMO heterostructures. However, this hypothesis needs to be verified by direct measurements of the ME coupling. As demonstrated above, the CFO sandwich layer in PZT/LSMO leads to higher interfacial trapped charges during the switching of the polarization in the PZT layer, which in turn affects the FM order parameter in the system. How the interplay between charge, spin, and polarization in novel PZT/CFO/LSMO heterostructures can combine to optimize ME response will also be an interesting subject of future investigation.

IV. CONCLUSIONS

In conclusion, PZT(200 nm)/CFO/LSMO(100 nm) heterostructures with the thickness of the CFO sandwich layer varying from 0 to 50 nm were grown on STO (100) substrates using an optimized pulsed laser deposition technique. Detailed x-ray diffraction and microscopy studies demonstrated the excellent quality of the heterostructures as well as the single-crystalline nature and epitaxial relationship of the individual layers with the substrates. The heterostructures with ultrathin (10–20 nm) CFO layers showed a simultaneous enhancement of ferromagnetic and ferroelectric properties as compared to PZT/LSMO. The higher magnetic saturation and coercivity in the CFO-containing samples was associated with the tetragonal distortion of the CFO lattice under epitaxial strain. A reorientation of the magnetic anisotropy in PZT/CFO/LSMO from out-of-plane (stabilized by tetragonal distortion of the unit cell) to in-plane (stabilized by shape anisotropy) as the thickness of the CFO sandwich layer increased was confirmed by a transverse susceptibility probe of the anisotropy fields in the system.

The enhanced ferroelectric coercive field was explained considering a model dielectric/FE (CFO/PZT) sandwich capacitor structure. Leakage and charging current characteristics showed the occurrence of charge injection from the LSMO electrodes into the dielectric CFO layer during voltage cycling. Trapped charge at the CFO/PZT interface generated an internal built-in field in the heterostructures, resulting in the accumulation of higher switched charges during voltage cycling and enhanced polarization in the CFO-containing heterostructures

over PZT/LSMO. The introduction of ultrathin CFO sandwich layers to improve both the ferromagnetic and ferroelectric properties of PZT/CFO/LSMO multiferroic heterostructures as reported in this work, along with a fundamental understanding of the structure-property relationships in the system, provides a template for the design and optimization of future magnetoelectric memory devices based on these and similar materials.

ACKNOWLEDGMENTS

This work was partially supported by the United States Army (Grant No. W81XWH1020101/3349). H.S. and M.H.P. acknowledge support from the U.S. Department of Energy, Office of Basic Energy Sciences, Division of Materials Sciences and Engineering under Award No. DE-FG02-07ER46438 (magnetic studies).

---

[1] R. Ramesh and N. A. Spaldin, Nat. Mater. **6**, 21 (2007).
[2] N. A. Spaldin and M. Fiebig, Science **309**, 391 (2005).
[3] S. W. Cheong and M. Mostovoy, Nat. Mater. **6**, 13 (2007).
[4] J. Ma, J. M. Hu, Z. Li, and C. W. Nan, Adv. Mater. **23**, 1062 (2011).
[5] N. A. Hill, J. Phys. Chem. B **104**, 6694 (2000).
[6] Y. Wang, J. M. Hu, Y. H. Lin, and C. W. Nan, Npg Asia Mater. **2**, 61 (2010).
[7] J. P. Zhou, Z. C. Qiu, and P. Liu, Mater. Res. Bull. **43**, 3514 (2008).
[8] M. Vopsaroiu, J. Blackburn, and M. G. Cain, J. Phys. D: Appl. Phys. **40**, 5027 (2007).
[9] M. Bibes and A. Barthelemy, Nat. Mater. **7**, 425 (2008).
[10] Y. Zhang, Z. Li, C. Deng, J. Ma, Y. Lin, and C.-W. Nan, Appl. Phys. Lett. **92**, 152510 (2008).
[11] J. X. Zhang, J. Y. Dai, and H. L. W. Chan, J. Appl. Phys. **107**, 104105 (2010).
[12] H. C. He, J. Wang, B. P. Zhou, and C. W. Nan, Adv. Funct. Mater. **17**, 1333 (2007).
[13] Z. Li, Y. Gao, B. Yang, Y. H. Lin, R. Yu, and C. W. Nan, J. Am. Ceram. Soc. **94**, 1060 (2011).
[14] C. A. F. Vaz, Y. Segal, J. Hoffman, R. D. Grober, F. J. Walker, and C. H. Ahn, Appl. Phys. Lett. **97**, 042506 (2010).
[15] S. Dussan, A. Kumar, J. F. Scott, and R. S. Katiyar, Appl. Phys. Lett. **96**, 072904 (2010).
[16] C. A. F. Vaz, J. Hoffman, Y. Segal, J. W. Reiner, R. D. Grober, Z. Zhang, C. H. Ahn, and F. J. Walker, Phys. Rev. Lett. **104**, 127202 (2010).
[17] J. M. Rondinelli, M. Stengel, and N. A. Spaldin, Nat. Nanotech. **3**, 46 (2008).
[18] J. Hoffman, X. Hong, and C. H. Ahn, Nanotechnology **22**, 254014 (2011).
[19] C. Thiele, K. Dorr, W. M. Lin, K. H. Muller, and L. Schultz, Sensor. Actuat. A-Phys. **129**, 180 (2006).
[20] L. Jiang, W. S. Choi, H. Jeen, S. Dong, Y. Kim, M. G. Han, Y. M. Zhu, S. V. Kalinin, E. Dagotto, T. Egami, and H. N. Lee, Nano Lett. **13**, 5837 (2013).
[21] F. Chen, Q. Z. Liu, H. F. Wang, F. H. Zhang, and W. Wu, Appl. Phys. Lett. **90**, 192907 (2007).
[22] X. D. Zhang, J. Dho, S. Park, H. Kwon, J. Hwang, G. Park, D. Kwon, B. Kim, Y. Jin, B. G. Kim, D. Karpinsky, and A. L. Kholkin, J. Appl. Phys. **110**, 064115 (2011).
[23] W. Chen, Z. H. Wang, W. Zhu, and O. K. Tan, J. Phys. D: Appl. Phys. **42**, 075421 (2009).
[24] N. Ortega, A. Kumar, R. S. Katiyar, and C. Rinaldi, J. Mater. Sci. **44**, 5127 (2009).
[25] H. C. He, J. Ma, Y. H. Lin, and C. W. Nan, J. Phys. D: Appl. Phys. **42**, 189802 (2009).
[26] D. Mukherjee, M. Hordagoda, P. Lampen, M.-H. Phan, H. Srikanth, S. Witanachchi, and P. Mukherjee, J. Appl. Phys. **115**, 17D707 (2014).
[27] D. Mukherjee, R. Hyde, M. Hordagoda, N. Bingham, H. Srikanth, S. Witanachchi, and P. Mukherjee, J. Appl. Phys. **112**, 064101 (2012).
[28] D. Mukherjee, T. Dhakal, R. Hyde, P. Mukherjee, H. Srikanth, and S. Witanachchi, J. Phys. D: Appl. Phys. **43**, 485001 (2010).
[29] D. Mukherjee, N. Bingham, M. Hordagoda, M. H. Phan, H. Srikanth, S. Witanachchi, and P. Mukherjee, J. Appl. Phys. **112**, 083910 (2012).
[30] D. Mukherjee, R. Hyde, P. Mukherjee, H. Srikanth, and S. Witanachchi, J. Appl. Phys. **111**, 064102 (2012).
[31] D. Mukherjee, N. Bingham, M.-H. Phan, H. Srikanth, P. Mukherjee, and S. Witanachchi, J. Appl. Phys. **111**, 07D730 (2012).
[32] F. Yang, N. Kemik, M. D. Biegalski, H. M. Christen, E. Arenholz, and Y. Takamura, Appl. Phys. Lett. **97**, 092503 (2010).
[33] S. Gariglio, N. Stucki, J. M. Triscone, and G. Triscone, Appl. Phys. Lett. **90**, 202905 (2007).
[34] R. M. Bozorth, E. F. Tilden, and A. J. Williams, Phys. Rev. **99**, 1788 (1955).
[35] P. D. Thang, G. Rijnders, and D. H. A. Blank, J. Magn. Magn. Mater. **310**, 2621 (2007).
[36] D. C. Jiles, J. Phys. D: Appl. Phys. **28**, 1537 (1995).
[37] T. Dhakal, D. Mukherjee, R. Hyde, P. Mukherjee, M. H. Phan, H. Srikanth, and S. Witanachchi, J. Appl. Phys. **107**, 053914 (2010).
[38] A. Lisfi, C. M. Williams, L. T. Nguyen, J. C. Lodder, A. Coleman, H. Corcoran, A. Johnson, P. Chang, A. Kumar, and W. Morgan, Phys. Rev. B **76**, 054405 (2007).
[39] H. Yanagihara, Y. Utsumi, T. Niizeki, J. Inoue, and E. Kita, J. Appl. Phys. **115**, 17A719 (2014).
[40] N. A. Frey, S. Srinath, H. Srikanth, M. Varela, S. Pennycook, G. X. Miao, and A. Gupta, Phys. Rev. B **74**, 024420 (2006).
[41] P. Poddar, J. L. Wilson, H. Srikanth, D. F. Farrell, and S. A. Majetich, Phys. Rev. B **68**, 214409 (2003).
[42] G. T. Woods, P. Poddar, H. Srikanth, and Y. M. Mukovskii, J. Appl. Phys. **97**, 10C104 (2005).
[43] A. Aharoni, E. H. Frei, S. Shtrikman, and D. Treves, Bull. Res. Counc. Isr. **6**, 215 (1957).
[44] L. Spinu, H. Srikanth, A. Gupta, X. W. Li, and G. Xiao, Phys. Rev. B **62**, 8931 (2000).
[45] A. I. Figueroa, S. Chandra, M. H. Phan, H. Srikanth, C. M. Bonilla, L. M. Garcia, F. Bartolome, J. Bartolome, and J. Herrero-Albillos, J. Appl. Phys. **109**, 07E118 (2011).

[46] N. A. Frey Huls, N. S. Bingham, M. H. Phan, H. Srikanth, D. D. Stauffer, and C. Leighton, Phys. Rev. B **83**, 024406 (2011).
[47] S. Chandra, N. A. F. Huls, M. H. Phan, S. Srinath, M. A. Garcia, Y. Lee, C. Wang, S. H. Sun, O. Iglesias, and H. Srikanth, Nanotechnology **25**, 055702 (2014).
[48] P. Zubko, D. J. Jung, and J. F. Scott, J. Appl. Phys. **100**, 114112 (2006).
[49] M. D. Nguyen, M. Dekkers, E. Houwman, R. Steenwelle, X. Wan, A. Roelofs, T. Schmitz-Kempen, and G. Rijnders, Appl. Phys. Lett. **99**, 252904 (2011).
[50] J. Schwarzkopf and R. Fornari, Prog. Cryst. Growth Charact. Mater. **52**, 159 (2006).
[51] I. H. Gul and A. Maqsood, J. Alloys Compd. **465**, 227 (2008).
[52] I. Stolichnov, in *Nanoscale Phenomena in Ferroelectric Thin Films*, edited by S. Hong (Kluwer Academic, New York, 2004).
[53] A. K. Tagantsev and I. A. Stolichnov, Appl. Phys. Lett. **74**, 1326 (1999).
[54] J. F. M. Cillessen, M. W. J. Prins, and R. M. Wolf, J. Appl. Phys. **81**, 2777 (1997).
[55] A. K. Tagantsev, C. Z. Pawlaczyk, K. Brooks, M. Landivar, E. Colla, and N. Setter, Integr. Ferroelectr. **6**, 309 (1995).
[56] I. Stolichnov and A. Tagantsev, J. Appl. Phys. **84**, 3216 (1998).
[57] L. Pintilie, I. Boerasu, M. J. M. Gomes, T. Zhao, R. Ramesh, and M. Alexe, J. Appl. Phys. **98**, 123104 (2005).
[58] I. K. Yoo, in *Nanoscale Phenomena in Ferroelectric Thin Films*, edited by S. Hong (Kluwer Academic, New York, 2004).
[59] J. F. Scott, in *Advanced Microelectronics Series*, edited by K. Itoh and T. Sakurai (Springer, Berlin, 2000).
[60] A. T. Bartic, D. J. Wouters, H. E. Maes, J. T. Rickes, and R. M. Waser, J. Appl. Phys. **89**, 3420 (2001).
[61] V. Y. Shur, E. L. Rumyantsev, E. V. Nikolaeva, E. I. Shishkin, and I. S. Baturin, J. Appl. Phys. **90**, 6312 (2001).
[62] V. Y. Shur, I. S. Baturin, E. I. Shishkin, and M. V. Belousova, Ferroelectrics **291**, 27 (2003).
[63] M. Dawber, K. M. Rabe, and J. F. Scott, Rev. Mod. Phys. **77**, 1083 (2005).
[64] G. Srinivasan, E. T. Rasmussen, B. J. Levin, and and R. Hayes, Phys. Rev. B **65**, 134402 (2002).
[65] X. Lv, C. Cheng, Y. Xiao, M. Tang, Z. Tang, H. Cai, Y. Zhou, and R. Li, Mater. Lett. **100**, 7 (2013).
[66] H. J. A. Molegraaf, J. Hoffman, C. A. F. Vaz, S. Garigilio, D. van der Marel, C. H. Ahn, and J. M. Triscone, Adv. Mater. **21**, 3470 (2009).